

Debonding monitoring of CFRP strengthened RC beams using active sensing and infrared imaging

Hoon Sohn*

*Department of Civil & Environmental Engineering,
Korea Advanced Institute of Science and Technology, Daejeon 305-701, Korea*

Seung Dae Kim[‡], Chi Won In^{††} and Kelly E. Cronin^{‡‡}

Carnegie Mellon University, Pittsburgh, PA 15213, USA

Kent Harries^{‡‡‡}

University of Pittsburgh, Pittsburgh, PA 15261, USA

(Received October 30, 2006, Accepted December 10, 2007)

Abstract. This study attempts to develop a real-time debonding monitoring system for carbon fiber-reinforced polymer (CFRP) strengthened structures by continuously inspecting the bonding condition between the CFRP layer and the host structure. The uniqueness of this study is in developing a new concept and theoretical framework of nondestructive testing (NDT), in which debonding is detected *without relying on previously-obtained baseline data*. The proposed reference-free damage diagnosis is achieved based on the concept of time reversal acoustics (TRA). In TRA, an input signal at an excitation point can be reconstructed if the response signal measured at another point is reemitted to the original excitation point after being reversed in the time domain. Examining the deviation of the reconstructed signal from the known initial input signal allows instantaneous identification of damage without requiring a baseline signal representing the undamaged state for comparison. The concept of TRA has been extended to guided wave propagations within the CFRP-strengthened reinforced concrete (RC) beams to improve the detectability of local debonding. Monotonic and fatigue load tests of large-scale CFRP-strengthened RC beams are conducted to demonstrate the potential of the proposed reference-free debonding monitoring system. Comparisons with an electro-mechanical impedance method and an inferred imaging technique are provided as well.

Keywords: active sensing; baseline-free nondestructive testing; carbon fiber reinforced polymer; debonding; structural health monitoring; time-reversal acoustics.

1. Introduction

Carbon fiber reinforced polymer (CFRP) composite materials have become an attractive alternate material for retrofit and rehabilitation of civil infrastructure systems due to their outstanding strength,

*Associate Professor, Corresponding Author, E-mail: hoonsohn@kaist.ac.kr

[‡]Ph.D. Candidate

^{††}Master Student

^{‡‡}Undergraduate Student

^{‡‡‡}Assistant Professor

light weight and versatility (Karbhari, *et al.* 2000). However, the improvement of strength and stiffness in a host structure can only be guaranteed when a reliable bonding condition between the host structure and the added CFRP materials is maintained. Therefore, a reliable nondestructive testing (NDT) system is required to monitor the initial installation quality and the long-term efficiency of bonding.

There is a large volume of research on damage detection techniques for FRP strengthened concrete structures. To name a few, acoustic emission (Mirmiran, *et al.* 1999), ultrasonic pulse velocities (Mirmiran and Wei 2001), infrared thermography (Levar and Hamilton 2003), fiber optic sensing (Ansari 2005), electromechanical (E/M) impedance spectrum (Giurgiutiu, *et al.* 2003), electrochemical impedance spectroscopy methods (Hong and Harichandran 2005), and microwave sensing (Akuthota, *et al.* 2004, Ekenel, *et al.* 2004, Feng, *et al.* 2000a) have been applied. These techniques are shown to successfully identify FRP debonding. However, data interpretation often needs to be manually performed by experienced engineers, and automation of data analysis remains largely unsolved. For continuous monitoring, it will be critical to reduce unnecessary interference by users and to automate the data analysis process as much as possible. In addition, although many damage detection techniques are successfully applied to scaled models or specimens tested in controlled laboratory environments, the performance of these techniques in real operational environments is still questionable and needs to be validated. Varying environmental and operational conditions produce changes in the system's dynamic response that can be easily mistaken for damage (Sohn 2007). It is challenging to develop a NDT technique with minimal false positive and negative indications of damage when the system is exposed to varying environmental and operational conditions. Few NDT systems have been developed with the intent of deploying it for continuous monitoring for in-service structures.

The ultimate goal of this study is to develop an NDT technique that goes beyond the laboratory demonstration and can be deployed in the field on real-world structures. To achieve this goal, a new NDT technique is developed by applying the concept of TRA (Fink and Prada 2001) to guided wave propagations (Rose 1999 and Viktorov 1967) within CFRP-strengthened RC beams. Based on TRA, an input signal at an excitation point can be reconstructed if the response signal measured at another point is reemitted to the original excitation point after being reversed in the time domain. This time reversibility is based on linear reciprocity of elastic waves, and breaks down when there is a source of nonlinearity along the wave propagation path. Because certain types of defects introduce nonlinear responses, examining the deviation of the reconstructed signal from the known initial input signal allows instantaneous identification of damage without requiring a direct comparison with previously-obtained baseline signal data. This novel concept is extended to develop a NDT system that can be rapidly deployed on laboratory specimens or in-field structures and autonomously perform local damage diagnoses at the presence of operational and environmental variation that in-service structures encounter. Smart materials such as lead zirconate titanate (PZT) are used for both generating and measuring guided waves (Giurgiutiu and Lyshevski 2004).

2. Wave propagation in target structures and time reversal acoustics

Elastic waves propagating in solid media can be classified into body and guided waves. All elastic waves including body and guided waves are governed by the same sets of Navier's partial differential equations (Rose 1999). The primary difference is that, while body waves are not constrained by any boundaries, guided waves need to satisfy the boundary conditions imposed by the physical systems as well as the governing equations. Guided waves can be further divided into Lamb, Stoneley and Rayleigh

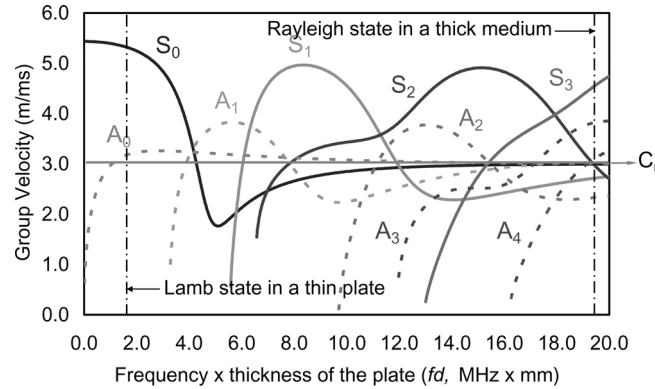


Fig. 1 A typical dispersion curve of Lamb wave in a thin plate

surface waves depending on specifics of the imposed boundary conditions.

Lamb waves are one type of guided waves that are constrained by two closely-spaced free surfaces (Viktorov 1967). In spite of its unique dispersion and multimode characteristics shown in Fig. 1, Lamb waves are widely used for defect detection in NDT applications due to their relatively long sensing range (Ing and Fink 1996, Kessler, *et al.* 2003, Kim and Sohn 2007, Mal, *et al.* 2005 and Sohn *et al.* 2007). However, as the thickness of the plate (or the product of the exciting frequency (f) and the thickness of the plate (d) in Fig. (1) increases, it becomes very hard to distinguish wave components because the fundamental symmetric (S_0) and anti-symmetric (A_0) Lamb modes converge to a Rayleigh surface wave (C_r) and additional higher symmetric and anti-symmetric modes appear.

Wave propagation characteristics are further complicated when a thin layer is attached to a thick medium. A RC beam with a CFRP layer is a good example of such a layered structure with two distinctively different thicknesses. Luangvilai, *et al.* (2002) experimentally obtained the dispersion curve of a concrete beam with a CFRP layer and demonstrated the complexity of its wave propagation characteristics. Therefore, a conventional Lamb wave approach may not be applicable for the monitoring of CFRP-RC beam coupled structures, and a new approach, which can be used regardless of the complexity of waves, is necessary. To address this issue, the concept of TRA is proposed.

The origin of the proposed time reversal process traces back to TRA (Fink and Prada 2001). This time reversibility of acoustic (or body) waves has found applications in lithotripsy, ultrasonic brain surgery, nondestructive evaluation, and acoustic communications (Fink 1999). The primary goal of the original TRA is to focus energy into a single point through the TRA. This TRA is further advanced by Park, *et al.* (2004) so that the shape of the original input signal can be preserved during the time reversal process. In this extended time reversal process, an input signal is applied at one point and the corresponding response is measured at another point. Then, the measured response is reversed in the time domain and applied back at the measurement point. Finally, the response at the initial excitation point is measured, and it can be showed that the shape of the final response signal should be identical to the original input signal. This final response signal is referred to as a reconstructed signal, and it is said that the time reversibility is preserved when the shape of the reconstructed signal is identical to the original input signal. However, the shape of the input signal is not well preserved for guided waves due to their multimode and dispersion characteristics.

A combination of a specific narrowband input waveform and multi-resolution signal processing is employed so that the time reversibility of guided waves is preserved within an acceptable tolerance for

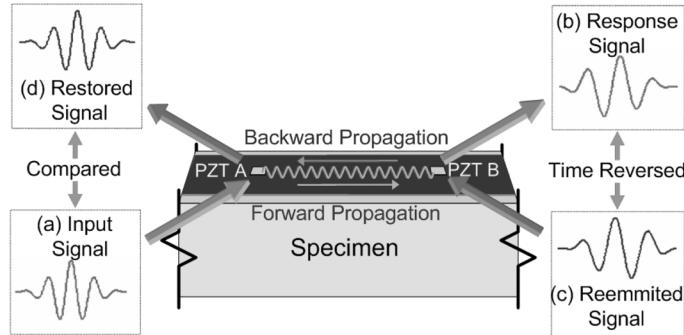


Fig. 2 Schematic concept of TRA-based damage identification that does not require any pas baseline signals: (a) a known input signal is applied to PZT A, (b) the corresponding response is measured at PZT B, (c) the response at PZT B is reversed in the time domain and applied back to PZT B, and (d) the final response is measured at PZT A. The shape of this reconstructed signal should be identical to the original input signal without defect along the wave propagation path.

more complex configurations such as the layered structure presented in this study (Park, *et al.* 2004). In the extended time reversal process, a narrowband input signal can be reconstructed at an excitation point (PZT A) if an output signal recorded at another point (PZT B) is reemitted to the original source point (PZT A) after being reversed and scaled in the time domain as shown in Fig. 2. Interested readers are referred to Kim, *et al.* (2007), where the extended time reversal process is described in detail.

Damage detection using the time reversal process is based on the premise that if there are certain types of defect along the wave propagation path, time reversibility breaks down. More precisely, the shape of the reconstructed signal’s main wave packet will depart from that of the original input signal and the symmetry of the reconstructed signal is violated. By examining the deviation of the restored signal’s main wave packet from the known input signal or the violation of the reconstructed signal’s symmetry as shown in Fig. 3, certain types of damage can be identified without requiring any previously obtained baseline signals. Based on this premise, two indices are proposed for damage identification: time reversibility (TR) and symmetry (SYM) indices. The TR index, defined below, compares the waveform of the original input with that of the reconstructed signal:

$$TR = 1 - \sqrt{\frac{\int_{t_i}^{t_r} I(t)V(t) dt}{\int_{t_i}^{t_r} I(t)^2 dt \int_{t_i}^{t_r} V(t)^2 dt}}^2 \tag{1}$$

where $I(t)$ and $V(t)$ denote the known input signal and the main wave packet in the reconstructed signal, respectively. For the experimental study presented, a 7-peak toneburst signal is used for excitation; t_i

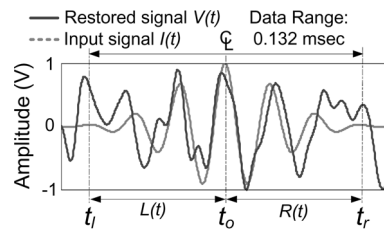


Fig. 3 Definition of t_i , t_o , and t_r used in Eqs. (1) & (2)

and t_r represent the starting and ending time points of the toneburst signal as defined in Fig. 3. The value of the TR index becomes zero when the shape of the main wave packet in the reconstructed signal is identical to that of the original input signal. Note that the amplitude scaling difference between $I(t)$ and $V(t)$ does not affect the TR value. If $V(t)$ deviates from $I(t)$, the TR index value increases and approaches 1.0, indicating the existence of damage along the wave propagation path.

The SYM index measures the degree of symmetry of the reconstructed signal with respect to the main wave packet in the middle.

$$\text{SYM} = 1 - \sqrt{\frac{\left\{ \int_{t_l}^{t_r} L(-t)R(t) dt \right\}^2}{\left\{ \int_{t_l}^{t_0} L(t)^2 dt \int_{t_0}^{t_r} R(t)^2 dt \right\}^2}} \quad (2)$$

where $L(t)$ and $R(t)$ denote the left-hand and right-hand sides of the reconstructed signal with respect to the main wave packet, t_0 is the center time point of the main wave packet and t_l and t_r represent the starting and ending time points as defined for the TR index. All terms are shown in Fig. 3.

Because time reversibility is based on the linear reciprocity of elastic waves, two guided waves, one propagating from PZT A to PZT B and the other from PZT B to PZT A, should be identical for the same input signal when the system stays in a linear regime. This linear reciprocity is shown to break down when a CFRP debonding along the wave path causes a nonlinear response. Furthermore, it is shown in our experiments that the anisotropic nature of the CFRP debonding breaks down the symmetry of the reconstructed signal. Therefore, the TR and SYM indices are used in the following experimental study to identify the initiation and propagation of CFRP debonding.

3. Descriptions of experiments

The overall configuration of the test specimens is shown in Fig. 4. A total of five specimens were tested for this study. Each RC beam was 254 mm deep, 152 mm wide and 4750 mm long. The first two beams are simply supported over 4267 mm and the last three beams are over 3962 mm. The beams were reinforced with 3 #4 (13 mm diameter) primary and 2 #3 (9 mm diameter) compression reinforcing bars. The soffit-applied preformed CFRP strip was 102 mm wide and 1.3 mm thick. A typical dimension of the specimen is shown in Fig. 4. The first two RC beams were fabricated from the same batch, and the CFRP strips were attached by a trained engineer. They were tested on October 14 and November 29-December 14, 2005. The additional three RC beams were manufactured on June 21, 2006, and the CFRP strips were glued by graduate students. In addition, a larger portion of epoxy materials were used for the first two specimens than for the last three specimens. Therefore, it is suspected that the bonding condition of the last three specimens be inferior to that of the first two specimens.

As shown in Fig. 4, three different measurement systems were employed in this experiment: active sensing, strain gauge and infrared imaging systems. Note that the E/M impedance method and infrared imaging were applied only to the last three specimens. For the last specimen, the infrared image was taken only at the beginning and end of the test.

A total of 15 square (2 cm × 2 cm × 0.0508 cm) PZT wafer transducers were attached on the free surface of the CFRP layer to form a distributed active sensing system (Fig. 4(b)). Here, PZT transducers were used for the proposed time reversal method and the E/M impedance method (Giurgiutiu, *et al.* 2003). The active sensing system (DAQ1 in Fig. 4(d)) was composed of an arbitrary function generator, a signal digitizer, and two multiplexers.

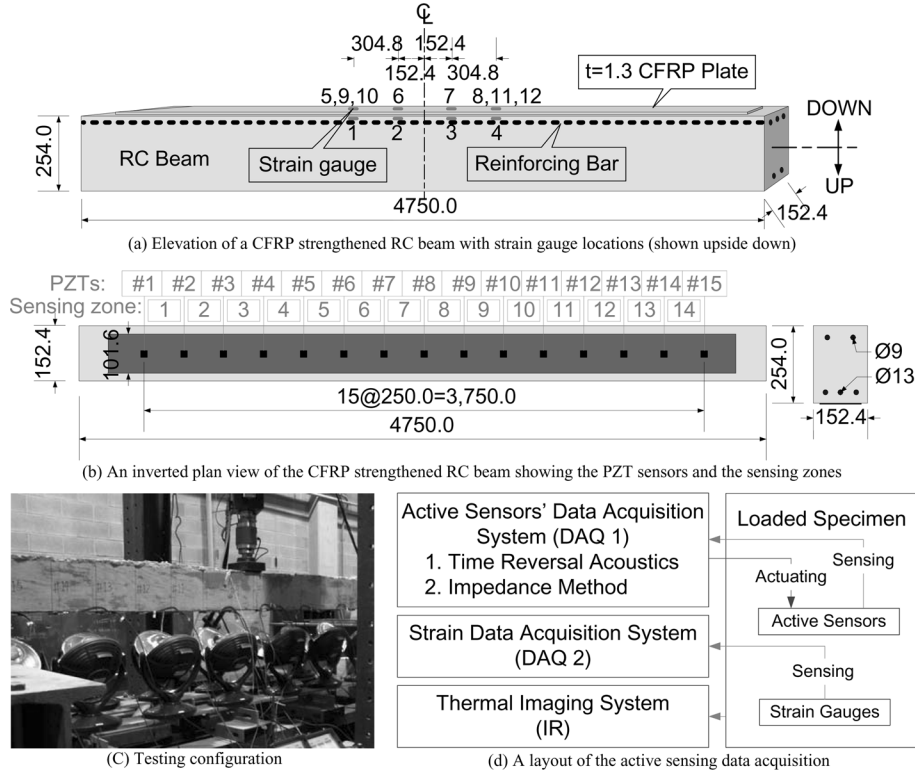


Fig. 4 Test setup and configuration of strain gauge and active sensing devices embedded/attached to the CFRP strengthened RC beam (all units are in mm)

For the time reversal method, excitation signals were applied to even number PZT wafers, and responses were measured at odd number PZTs. For instance, a 7-peak toneburst signal was applied to PZT #2, and the corresponding forward signal was measured at PZT #1. Then, the measured forward signal was time-reversed and applied at PZT #2 again, and the reconstructed signal was measured at PZT #1. This time reversal process was repeated for a total of 14 different path combinations (PZTs #2–#1, PZTs #2–#3, ..., and PZTs #14–#15). These 14 sensing segments were referred to as sensing zones #1 to #14 in Figure 4(b). The driving frequency value and the sampling rate of the digitizer were set to 45 kHz and 5 MHz, respectively. The data collection for all 14 sensing zones took about 3 minutes. Each forwarding and time reversed signals were averaged 10 times in the time domain to minimize the effect of noise and to improve the signal-to-noise ratio.

For the E/M impedance method, a chirp signal in a frequency range of 1 kHz to 50 kHz was used as an excitation. Each PZT wafer was actuated and sensed sequentially from PZTs #1 through #15 with the chirp signal. The E/M impedance technique measures the high-frequency local impedance of the structure through the PZT wafer transducers coupled to the structure (Giurgiutiu and Zagari 2001). When a PZT wafer is excited with a broadband input, the impedance peaks associated with structural resonances appears in the real part of the complex impedance (Giurgiutiu, *et al.* 2003). It is expected that debonding of a CFRP layer create additional structural resonances and the appearance of these resonances can be detected by the impedance measure. It took about 3.5 minutes to measure and compute the E/M impedance for all 15 PZTs. Time-averaging similar to the previous time reversal

method was conducted as well.

The temperature change on the CFRP surface was measured using an infrared camera, because it was reported that the heat convection rate of the CFRP layer depends on the bonding condition of the CFRP with the concrete substrate (Jackson, *et al.* 1999, Levar and Hamilton 2003, Starnes, *et al.* 2003). Infrared images were taken using a commercial infrared camera (ThermaCAM S40). Detailed specifications for the infrared camera include; (1) field of view/min focus distance: 24°×18°/0.3 m; (2) spatial resolution (IFOV): 1.3 mrad; (3) image frequency: 60 Hz; (4) thermal sensitivity @ 50/60 Hz: 0.08 °C at 30 °C; (4) detector type: focal plane array (FPA) uncooled microbolometer 320×240 pixels; (5) temperature ranges: -40 °C to +120 °C; and (5) accuracy (% of reading): ±2 °C or ±2%. The images were stored on a laptop computer and processed by a software program called ThermaCAM Researcher Pro 2.7. As shown in Fig. 4(c), 14 commercial heaters were placed under the test specimen. Each heater was able to cover each sensing zone. First, each sensing zone was heated for about 20 seconds using an individual heater, and it was turned off. Then, a thermal image was taken. It took about 7 minutes to scan the entire specimen (sensing zones #1 to #14). For the monotonic test cases (Cases V-VII), the images from all 14 sensing zones were taken until the loading of the hydraulic actuator reached to 40.03 kN. Then, loading was switched from a force-control to a displacement control. Once it was switched to displacement control, only sensing zones #5 to #10 were scanned to reduce data collection time. Note that because the loading continuously increased even during scanning of the specimen, it was important to minimize the data collection time to protect the camera. When the loading reached to a level at which initial debonding was expected to start, only a few selected sensing zones were inspected with the infrared camera. The final images were taken when the loading test was completed.

The strain data acquisition system (DAQ2 in Fig. 4(d)) includes four electrical resistance strain gauges on the internal reinforcing steel bars and four additional strain gauges mounted on the surface of the CFRP layer coincident with the previous strain gauges. These instruments were used to measure strains and to identify the presence of debonding at the discrete gauge locations. Details of the experimental setup and data analysis results based on strain measurements can be found in Reeve (2005) and Zorn (2006).

Seven loading cases were investigated in this study (Cases I-VII) using five specimens. The loading condition, specimen number and NDT methods used for each case are summarized in Table 1. For all cases, loading was applied at the mid-point of the simply supported beam. The loading was initially applied in a force-control manner and subsequently switched to a displacement control. During the force-control of the monotonic tests and the fatigue tests, the loading was held constant to collect data from the active sensing system. On the other hand, data necessary for the time reversal and impedance methods were continuously collected during the displacement control of the monotonic tests.

Table 1 A summary of experimental tests, loading conditions, used specimens and NDT methods

Case #	Specimen #	Loading	Used NDT techniques ¹
I	1	Monotonic	
II	2	Fatigue	ST, TR
III	2	Monotonic	ST, TR
IV	3	Fatigue	ST, TR, IM
V	3	Monotonic	ST, TR, IM, IR
VI	4	Monotonic	ST, TR, IM, IR
VII	5	Monotonic	ST, TR, IM, IR ²

¹TR (time reversal acoustics), IM (impedance method), IR (infrared thermography), and ST (strain measurement); ² The infrared image was taken only at the beginning and end of the test.

In Case I (Specimen L4 reported in Reeve 2005), the first specimens was subjected to incremental monotonic loading, and the data from the active sensing system were collected at each loading step. The monotonic load was gradually increased until the specimen failed. The loading was initially force-controlled up to loading step 5 (40.03 kN) and then switched to a displacement control as the beam “yielded” starting from loading step 6 (41.59 kN) to loading step 24 (44.54 kN).

The second specimen (Specimen L4F reported in Zorn 2006) was first subjected to fatigue loading in Case II and subsequently to monotonic loading to failure in Case III. In Case II, the cyclic load ranged from 4.45 kN to 22.24 kN, and it was operated with a driving frequency of 1.7 Hz. The specimen underwent a total of 2,000,000 fatigue load cycles over 16 days. Data from the active sensing system were gathered at several loading cycles: N=0, 1, 100, 200, 500, 1000, 2000, 5000, 10000, 162330, 308800, 439880, 609490, 721990, 891160, 1030700, 1175690, 1321900, 1428920, 1564430, 1651580, 1786920, 1896400, 2000000 cycles.

A monotonic load test similar to Case I was performed on the second specimen following the fatigue-conditioning described above. This was referred to as Case III. Data were measured at 14 loading steps (13.34 kN to 48.11 kN). The force controlled loading was initially applied up to loading step 4 (36.90 kN), and the loading was changed to the displacement control up to loading step 14 (48.11 kN). Details for the first three cases (Cases I-III) can be found in Kim, *et al.* (2007). For Case I-III, data only for the time reversal method and strain gauge measurements were collected. It is worthwhile to mention the unique contribution of this work in comparison with Kim, *et al.* (2007). While only the damage diagnosis using TRA were reported for Cases I-III in Kim, *et al.* (2007), additional specimen tests (Cases IV-VII) were conducted in this study and compared with the impedance and infrared imaging techniques.

Similar to the second specimen, the third specimen was first subjected to fatigue loading in Case IV and subsequently to monotonic loading up to failure in Case V. For Case IV, the specimen underwent a total of 2,000,000 fatigue load cycles over 14 days. Data from the active sensing system were gathered at several loading cycles: N = 0, 1, 100, 200, 500, 1000, 2000, 5000, 10000, 300000, 450000, 600000, 707000, 900000, 1040000, 1210000, 1392000, 1540000, 1700000, 1840000, 2000000 cycles. The driving frequency of the fatigue loading was set to 2.0 Hz to reduce total experimental time. During the fatigue loading test, the load was paused at the minimum load of 4.45 kN at several cycles to collect data necessary for the time reversal and impedance methods using the active sensing system. After the completion of Case IV, a monotonic load test (Case V) similar to Cases III was performed on the same specimen. The test configuration of Case V was similar to that of Case III. Time reversal signals, impedance data and thermal images were collected at 12 incremental loading steps.

Similar to Cases I, III and V, two additional specimens (specimens #4 and #5) were subjected to incremental monotonic loading in Cases VI and VII. These two specimens were incrementally loaded until failure, and they failed at 58.47 kN (loading step 10) and 46.28 kN (loading step 16), respectively. Active sensing data and thermal images were collected at all 10 loading steps in Case VI. Similarly, active sensing data for the time reversal and impedance methods were collected at all 16 loading steps in Case VII, but the infrared image was captured only after the completion of the test because of concerns regarding the infrared camera safety.

4. Experimental results

Experimental results from the proposed time reversal technique, the E/M impedance method and the infrared imaging technique are reported here. The proposed time reversal method was applied during

all test cases (Cases I-VII) while the impedance method and the infrared imaging were applied for Cases IV-VII and Cases V-VII, respectively. For all cases, visual inspection and a coin-tapping test were conducted at the beginning and end of each case. The final debonded areas identified by the visual inspection (including a coin-tapping test) are shown in Fig. 5.

4.1. Time reversal method

The damage diagnosis obtained from Case I-III is presented from Fig. 6 to Fig. 9. In Fig. 6, the TR and SYM indices are shown along the length of the beam and computed at selective loading steps (loading steps 1, 2, 6, 7, 15 and 24) of Case I. As reported in Kim, *et al.* (2007), the initial increase of the TR and SYM indices at the mid-span did not result from debonding but rather from initial cracking of the concrete beam near a 4.8 mm diameter steel rod, which was embedded in the concrete to connect the midspan displacement transducer. The initial abnormal increases of these index values disappeared when the steel rod was removed in Case IV-VII. The TR and SYM indices values at sensing zones #10 and #14 are plotted as a function of the 24 loading steps in Fig. 7. Fig. 7 shows that the TR and SYM indices significantly increased at loading step 5 near sensing zone #10. Overall, the findings from Case I agreed well with the visual inspection result presented in Fig. 5 and the data obtained from the strain

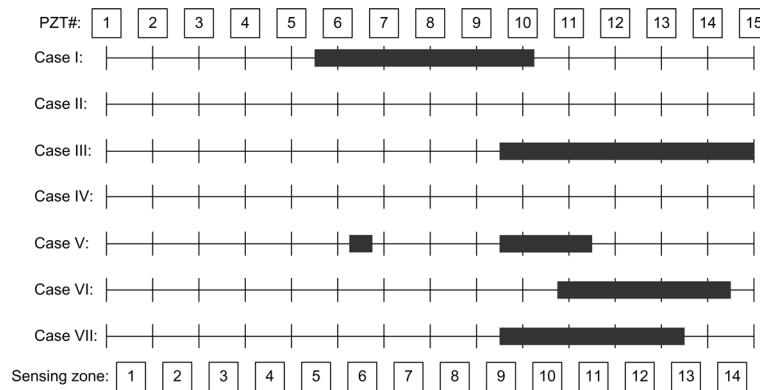


Fig. 5 Debonding areas estimated from visual inspection and a coin tapping test performed at the completion of each loading case (the dark solid bar represents the estimated debonding area)

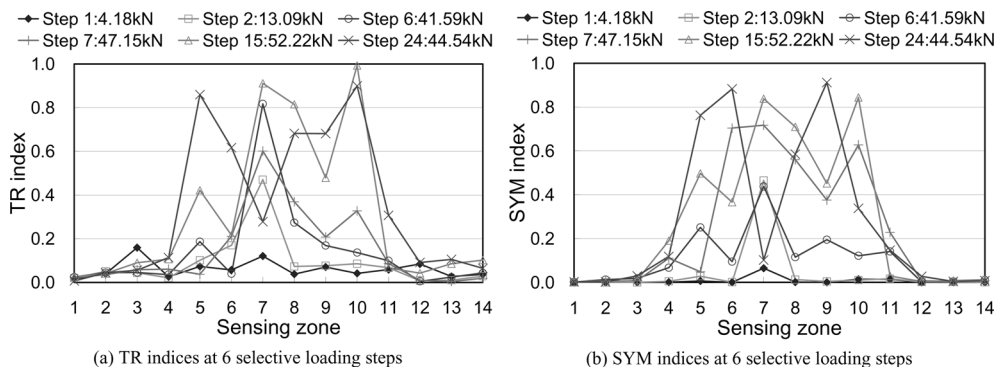


Fig. 6 Changes of the TR and SYM indices measured at selective loading steps during the Case I monotonic loading test

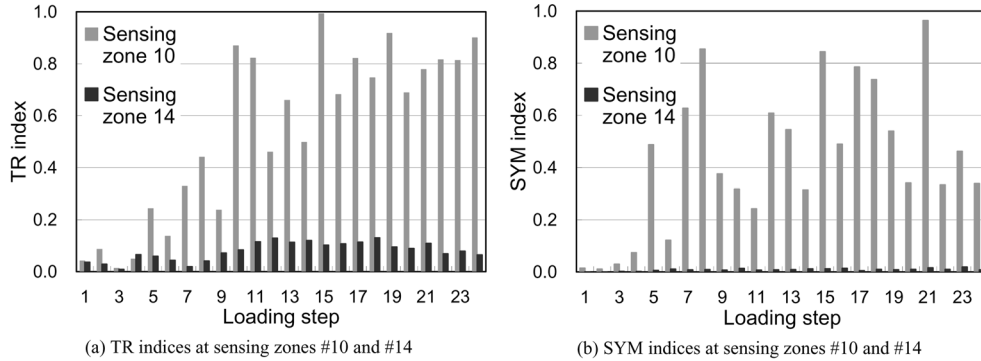


Fig. 7 Changes of TR and SYM indices as a function of incremental monotonic loading measured at sensing zones #10 and #14 for Case I

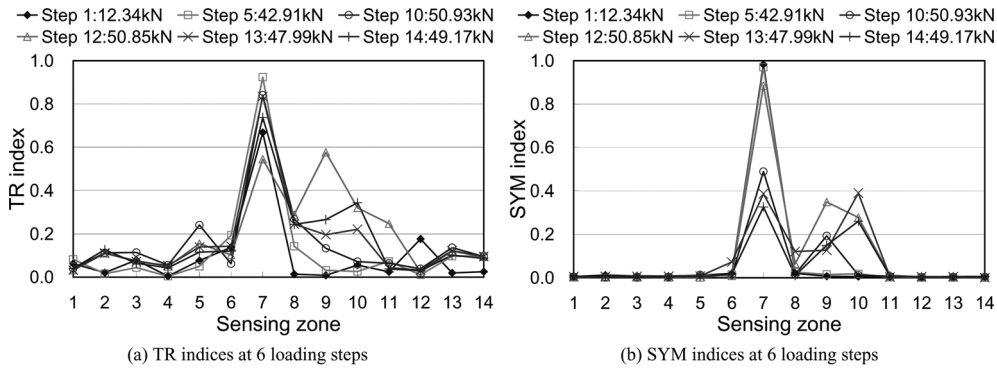


Fig. 8 Changes of the TR and SYM indices measured at selective loading steps during the Case III monotonic loading test

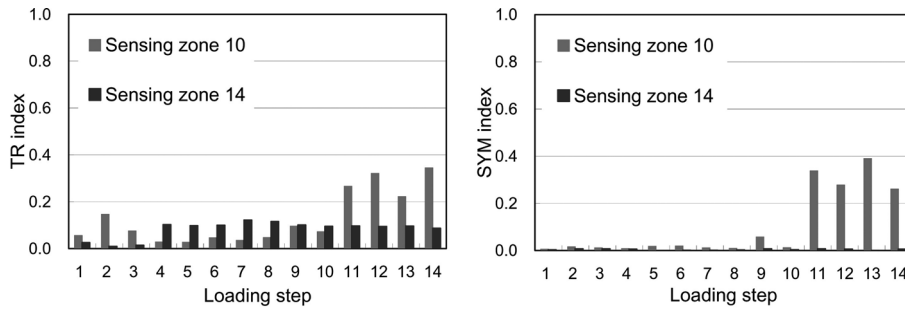


Fig. 9. Change of the TR and SYM indices as a function of increasing monotonic loading measured at sensing zone #10 and #14 for Case III

gauge system (Reeve 2005).

The second specimen was subjected to fatigue loading in Case II and subsequently to monotonic loading in Case III. In Case II, no sign of CFRP debonding was found and it was substantiated by the visual inspection performed at the end. In Case III, the TR and SYM indices shown in Fig. 8 and Fig. 9 successfully identified debonding near sensing zone #10 at loading step 11. The debonding became visible around at loading step 13. Therefore, Case III showed that the proposed method might provide

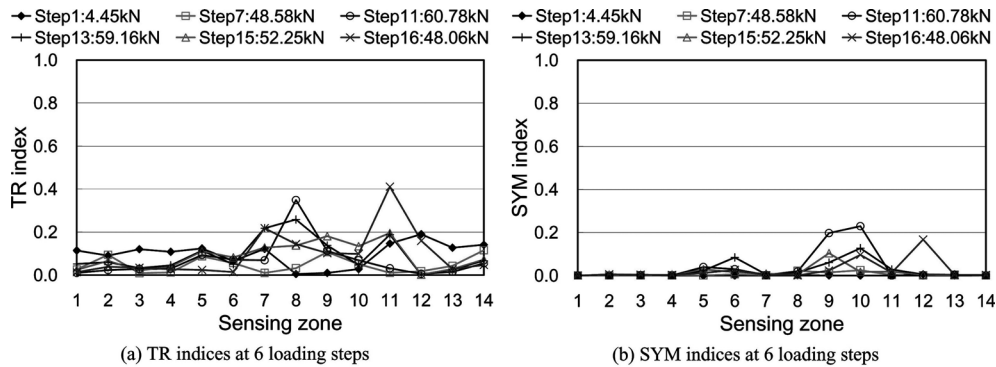


Fig. 10 Changes of the TR and SYM indices measured at selective loading steps during the Case VII monotonic loading test

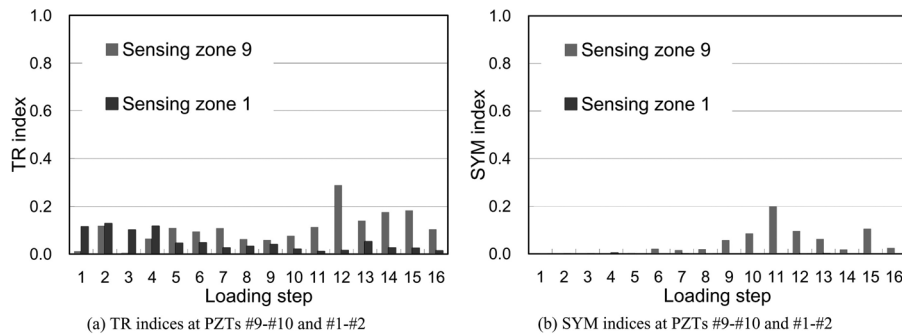


Fig. 11 Change of the TR and SYM indices as a function of increasing monotonic loading measured at sensing zone #9 and #1 for Case VII

an early warning of debonding before visual inspection could identify debonding. Similar to Case II, the specimen of Case IV was subjected to fatigue loading. No sign or evidence of CFRP debonding was found during the test of Case IV.

For the remaining three monotonic loading cases (Cases V, VI and VII), the observed failure mechanisms were qualitatively similar to each other. In all three cases, debonding started around sensing zone #9 and propagated toward sensing zone #14. A representative result from Case VII is presented in Figure 10 and Fig. 11. Fig. 10 shows the TR and SYM indices measured at selective loading steps (1, 7, 13, 14, 15 and 16) during the Case VII monotonic loading test. In contrast to Fig. 6 and Fig. 8, the initial increases of the TR and SYM indices at the mid-span were not observed in Fig. 10. From this result, it was verified that the initial abnormal TR and SYM indices for Case I-III were caused by the steel rod embedded in the middle of the beam.

Although the visual inspection of Case VII indicated that debonding ranged from sensing zone #9 to #13, the TR and SYM indices increased only at a subset of the actually debonded areas. Furthermore, the TR and SYM indices from the same sensing zones were sometimes inconsistent. For example, the TR index value at sensing zone #11 was over 0.4 at loading step 16, but the corresponding SYM index remained close to zero in Fig. 10. A similar type of inconsistency was also observed in the Fig. 11, which plotted the TR and SYM indices values at sensing zones #1 and #9 as a function of the 16 loading steps. These sensing zones were selected, because debonding initiated from sensing zone #9 and no debonding was expected at sensing zone #1 located at the end of the beam. Fig. 11 shows that:

(1) The TR and SYM indices significantly increased at loading steps 11 and 12 near sensing zone #9, but they decreased and went back to the original values finally; (2) The sudden increases of the TR and SYM indices correspond well with the initiation time of the actual debonded area, and a similar increase had been observed in Case III; (3) The decreases of the TR and SYM indices after the initial increase were not seen in the previous test cases; (4) the values of these indices did not vary much near sensing zone #1 throughout the entire test. This result was consistent with Cases I and III.

It is speculated that the debonding diagnoses for the last three specimens were not as good as for the first two specimens because prominent nonlinearity were not necessarily produced during the CFTP debonding of these specimens. While the CFRP strips for the first two specimens were attached by a trained engineer, graduate students glued the CFRP strips for the last three specimens. Furthermore, a larger portion of epoxy adhesive was used for bonding CFRP layers in the first two specimens than in the last three specimens. Therefore, the top portion of the concrete layer came off with the CFRP layer when debonding was introduced in the first two specimens. Subsequently, the anisotropic nature of the debonded area was believed to produce nonlinear response. On the other hand, debonding was initiated at the interface between the CFRP layer and the concrete surface for the last three specimens without causing prominent nonlinearity. Because the proposed time reversal method was designed to detect nonlinear responses introduced by debonding, it was speculated that debonding was not well identified for the last three specimens.

4.2. E/M impedance method

The E/M impedance method was applied to Case IV-VII. Fig. 12 shows the PZTs #9 and #12 impedance values measured at loading steps 1 and 15 and after the completion of the Case VII monotonic loading test. Note that PZTs #9 and #12 are at the boundary of sensing zone #9 and #12, respectively. In contrast to the time reversal method which depends on the generation of the material nonlinearity resulted from debonding, the E/M impedance method detects CFRP debonding based on additional resonances that appear in the impedance measure. After the completion of the test, it was confirmed that sensing zone #9 was partially debonded and sensing zone #12 was fully debonded. However, no remarkable change in the PZT #9 impedance measure was shown in Fig. 12(a). On the other hand, multiple resonances appeared in the PZT #12 impedance shown in Fig. 12(b) when the CFRP layer was fully debonded from the concrete substrate. Similar results were observed in the other PZT impedance measures, and they were consistent with the experimental results reported in Giurgiutiu *et al.* (2003). However, debonding was detected only after the completion of the test although debonding was already visible at loading step 15.

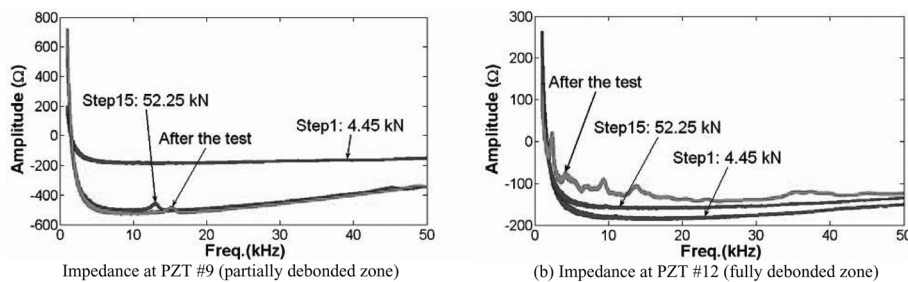


Fig. 12 The PZT impedances measured at selective loading steps during the Case VII monotonic loading test

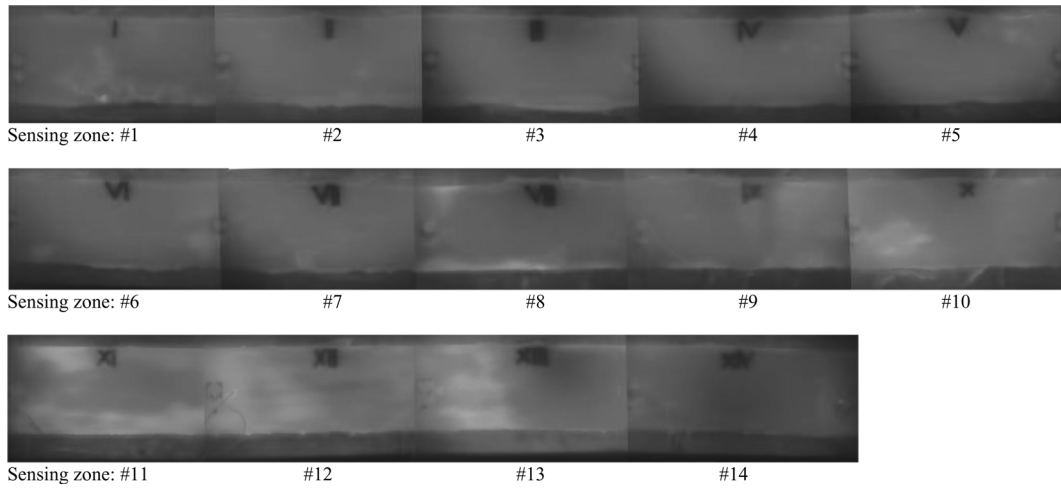


Fig. 13 Infrared images taken after the completion of Case VII (Actual debonding are: sensing zones #9 to #13)

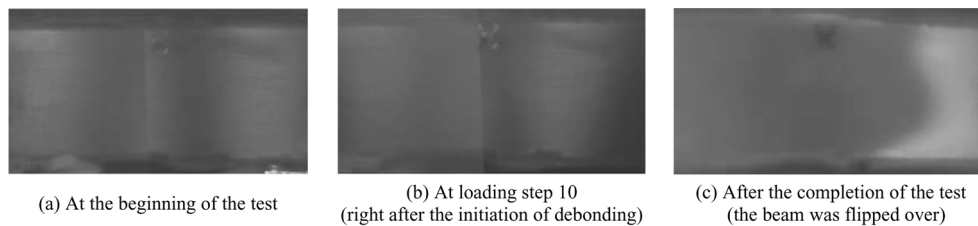


Fig. 14 Comparison of IR images taken from sensing zone #10 at three different loading steps of Case VI: (a) at the beginning of the test, (b) right after the initiation of debonding, and (c) after the completion of the test

4.3. Infrared imaging technique

The infrared thermal images taken from Cases VII and VI are shown in Fig. 13 and Fig. 14, respectively. The brighter color in the infrared image shows a region of higher temperature, and this is caused by a slower heat convection due to CFRP debonding. That is, a region with a brighter color presented an area of debonding. Fig. 13 shows a good agreement with the debonding area estimated from the visual inspection conducted at the completion of the test shown in Fig. 5. A brighter area within sensing zone #8 was caused by not putting enough epoxy materials between the CFRP and the RC beam initially. As long as there were a gap between the CFRP layer and the concrete substrate, the infrared imaging technique successfully identified debonding. However, debonding was not visible in the infrared image when the test specimens were subjected to loading. When the beam was still subjected to the monotonic loading, the gap between the CFRP layer and the RC beam was closed even at the presence of debonding. This loading prevented debonding from appearing in the infrared image. For instance, Fig. 14 (a) and (b) show the thermal images of sensing zone #10 taken at the beginning and loading step 10 of Case VI, respectively. Although debonding was visually apparent at loading step 10, it was not visible in Fig. 14(b). Fig. 14(c) was taken once the loading was removed and the specimen was placed on the floor. In this condition, debonding became apparent.

These findings are inline with the previous studies reported by Levar and Hamilton (2003) and

Starnes, *et al.* (2003), in which the thermal images were taken from unloaded conditions. During the test, several drawbacks of the infrared imaging method were identified: (1) infrared images should be interpreted by users, (2) it requires a high resolution infrared camera and additional heating devices, (3) it may not be applicable to areas where only limited access is available and (4) it may not be suitable for continuous monitoring.

5. Conclusions

In this study, a continuous monitoring system for detecting CFRP debonding from a host reinforced concrete structure is developed, and its performance is compared with other prevailed NDT techniques. The uniqueness of this study is in developing a new concept and theoretical framework of a *baseline-free* NDT. The applicability of this *baseline-free* NDT technique to monitoring of CFRP debonding was investigated through seven loading cases of five CFRP strengthened RC beam specimens: three monotonic loading tests (Cases I, VI and VII), two fatigue loading tests (Cases II and IV), and two monotonic loading tests following the fatigue loading tests (Cases III and V).

The proposed approach successfully estimated the initiation and the regions of debonding in Cases I-III. However, only the initiation of debonding was reliably identified in Cases IV-VII. While the first two specimens were fabricated from the same batch and the CFRP strips were attached by a trained engineer, the last three specimens were manufactured from a different batch and the CFRP strips were glued by graduate students. When debonding was introduced in the first two specimens, the top concrete layer came off with the CFRP layer due to a strong bonding between the CFRP layer and the concrete beam. On the other hand, debonding was initiated at the interface between the CFRP layer and the concrete surface for the last three specimens as a result of the poor workmanship during the initial bonding process. Nonlinear response characteristics observed in the debonding cases of the first two specimens were not evident in the last three specimens. Because the proposed time reversal methods is designed to detect nonlinear responses introduced by debonding, it is speculated that the debonding was not well identified for the last three specimens.

Different from the time reversal method which detects nonlinearity resulted from debonding, the E/M impedance method monitors the change of the E/M impedance caused by debonding. The R/M impedance method successfully identified the fully debonded areas as long as the CFRP layer is physically separated from the concrete substrate and produces distinctive resonance frequencies. However, it was difficult to detect partial or fully debonded areas unless there was a clear gap between the CFRP layer and the concrete substrate.

The outcome of the infrared imaging was similar to that of the E/M impedance method. The temperature contour of the CFRP surface was measured by the infrared camera. It was observed that a gap between the CFRP layer and the concrete altered the local heat convection rate and produced temperature variation on the CFRP surface. However, this temperature change was only visible when the CFRP layer was physically apart from the concrete substrate.

The experimental results demonstrated the potential advantage of adopting the time reversal process for damage diagnosis over the other NDT approaches investigated: The proposed approach was able to monitor debonding in a larger area than conventional strain gauges or impedance measurements, which provide only discrete points or near-field measurements. In addition, the proposed technique might be more suitable for continuous field deployment than infrared imaging.

Finally, further research is warranted to better understand the exact sources of nonlinearity. Although

this study demonstrated that CFRP debonding from the substrate concrete media might introduce nonlinear responses, this finding depended on the initial bond condition of the CFRP layer. At this point, it is unclear how exactly the bonding condition or debonding mechanism affect nonlinear wave propagation responses.

Acknowledgements

This research was supported under the US NSF Grant No. CMS-0529208, the Korea Science and Engineering Foundation (M20503000015-07N0300-01510), and the Korea Research Foundation (D00462). The beam testing for Cases I-III was conducted by Andrew Zorn and Benjamin Reeve in the Watkins-Haggart Structural Engineering Laboratory at University of Pittsburgh. The infrared camera used during Cases V-VII were provided by Professor Minking Chyu in the Department of Mechanical Engineering at University of Pittsburgh, and the infrared imaging tests were assisted by Mr. Sean Siw at University of Pittsburgh.

References

- Akuthota, B., Hughes, D., Zoughi, R., Myers, J. and Nanni, A. (2004), "Near-field microwave detection of disbond in carbon fiber reinforced polymer composites used for strengthening cement-based structures and disbond repair verification", *J. Mater. Civil. Eng.*, **16**(6), 540-546.
- Ansari, F. (2005), "Fiber optic health monitoring of civil structures using long gage and acoustic sensors", *Smart Mater. Struct.*, **14**(3), S1-S7.
- Ekenel, M., Stephen, V., Myers, J. J. and Zoughi, R. (2004), "Microwave NDE of RC beams strengthened with CFRP laminates containing surface defects and tested under cyclic loading", *Proc., 16th World Conference on Nondestructive Testing*, Montreal, Canada. August 30-September 3.
- Feng, M. Q., Flaviis, F. and Kim, Y. J. (2000a), "Use of microwaves for damage detection of fiber reinforced polymer-wrapped concrete structure", *J. Eng. Mech.*, **128**(2), 172-183.
- Fink, M. (1999), "Time-reversed acoustics", *Scientific American*, **281**(5), 91-97.
- Fink, M. and Prada, C. (2001), "Acoustic time-reversal mirrors", *Inverse Problems*, **17**, R1-R38.
- Giurgiutiu, V. and Zagari, A. N. (2001), "Embedded self-sensing piezoelectric active sensors for online structural identification", *ASME Journal of Vibration and Acoustics*, **124**, January 116-125
- Giurgiutiu, V., Harries, K. A., Petrou, M. F., Bost, J. and Quattlebaum, J. (2003), "Disbond detection with piezoelectric wafer active sensors in RC structures strengthened with FRP composite overlays", *Earthquake Eng. And Eng. Vib.*, **2**(2), 213-224.
- Giurgiutiu, V. and Lyshevski, S. E. (2004), *Micromechatronics: Modeling, analysis, and design with MATLAB*, CRC Press Inc, Boca Raton, FL.
- Hong, S. and Harichandran, R. (2005), "Sensors to monitor CFRP/concrete bond in beams using electrochemical impedance spectroscopy", *J. Compo. Constr.*, **9**(6), 515-523.
- Ing, R.K. and Fink, M. (1996), "Time recompression of dispersive lamb waves using a time reversal mirror – application to flaw detection in thin plates", *Proc., 1996 IEEE Ultrasonics Symposium*, **1**, 659-663.
- Jackson, D. R., Islam, M., Hurley, T. J. and Alvarez, F. J. (1999), "Feasibility of evaluating fiber reinforced plastic (FRP) wrapped reinforced concrete columns using ground penetrating radar (GPR) and infrared (IR) thermography", *Demonstration Project No.*, 84-2, U.S. Department of Transportation-Federal Highway Administration, Washington, D.C.
- Karbhari, V. M., Chin, J. W. and Reynaud, D. (2000), "Critical gaps in durability data for FRP composites in civil infrastructure", *Proc., 45th International Society for the Advancement of Materials and Process Engineering (SAMPE) Symposium and Exhibition*, Vol. 45, 549-563, Long Beach, CA, May 21-25.

- Kessler, S. S., Johnson, C. E. and Dunn, C. T. (2003), "Experimental application of optimized Lamb wave actuating/sensing patches for health monitoring of composite structures", *Proc., of the 4th International Workshop on Structural Health Monitoring*, Stanford University, 429-436.
- Kim, S. B. and Sohn, H. (2007), "Instantaneous reference-free crack detection based on polarization characteristics of piezoelectric materials", *Smart Mater. Struct.*, **16**, 2375-2387.
- Kim, S. D., In, C. W., Cronin, K., Sohn, H. and Harries, K. (2007), "A reference-free NDT technique for debonding detection in CFRP strengthened RC structures", *ASCE J. Struct. Eng.*, **133**(8), 1080-1091.
- Levar, J. and Hamilton, H. (2003), "Nondestructive evaluation of carbon fiber-reinforced polymer-concrete bond using infrared thermography", *ACI Mater. J.*, **100**(1), 63-72.
- Luangvilai, K., Punurai, W. and Jacobs, L. (2002), "Guided lamb wave propagation in composite plate/concrete component", *J. Eng. Mech.*, **128**(12), 1337-1341.
- Mal, A. K., Shih, F. J., Ricci, F. and Sauvik, B. (2005), "Impact damage detection in composite structures using Lamb waves", *Proc., of the SPIE*, **5768**, 295-303.
- Mirmiran, A., Shahawy, M. and Echary, H. (1999), "Acoustic emission monitoring of hybrid FRP-concrete columns", *J. Eng. Mech.*, **125**(8), 899-905.
- Mirmiran, A. and Wei, Y. (2001), "Damage assessment of FRP-encased concrete using ultrasonic pulse velocity", *J. Eng. Mech.*, **127**(2), 126-135.
- Park, H. W., Sohn, H., Law, K. H. and Farrar, C. R. (2004), "Time reversal active sensing for health monitoring of a composite plate", *J. Sound Vib.*, in press.
- Reeve, B. (2005), "Effect of adhesive stiffness and CFRP geometry on the behavior of externally bonded CFRP retrofit measures subject to monotonic loads", MS Thesis, University of Pittsburgh Department of Civil and Environmental Engineering.
- Rose, L. J. (1999), *Ultrasonic Waves in Solid Media*, Cambridge University Press, New York.
- Sohn, H., (2007), "Effects of environmental and operational variability on structural health monitoring", *A Special Issue of Philosophical Transactions of the Royal Society on Structural Health Monitoring*, **365**, 539-560.
- Sohn, H., Park, H., Law, K. and Farrar, C. (2007), "Combination of a time reversal process and a consecutive outlier analysis for baseline-free damage diagnosis", *J. Intell. Mater. Sys. Struct.*, **18**(4), 335-346.
- Starnes, M. A., Carino, N. J. and Kausel, E. A. (2003), "Preliminary thermography studies for quality control of concrete structures strengthened with fiber-reinforced polymer composites", *J. Mater. Civil Eng.*, **15**(3), 266-273.
- Viktorov, I. A. (1967), *Rayleigh and Lamb Waves*, Plenum Press, New York.
- Zorn, A. (2006), "Effect of adhesive stiffness and CFRP geometry on the behavior of externally bonded CFRP retrofit measures subject to fatigue loads", MS Thesis, University of Pittsburgh Department of Civil and Environmental Engineering.